The American Journal of Human Genetics, Volume *102*

Supplemental Data

Patient-iPSC-Derived Kidney Organoids Show Functional Validation of a Ciliopathic Renal Phenotype and Reveal Underlying Pathogenetic Mechanisms

Thomas A. Forbes, Sara E. Howden, Kynan Lawlor, Belinda Phipson, Jovana Maksimovic, Lorna Hale, Sean Wilson, Catherine Quinlan, Gladys Ho, Katherine Holman, Bruce Bennetts, Joanna Crawford, Peter Trnka, Alicia Oshlack, Chirag Patel, Andrew Mallett, Cas Simons, and Melissa H. Little

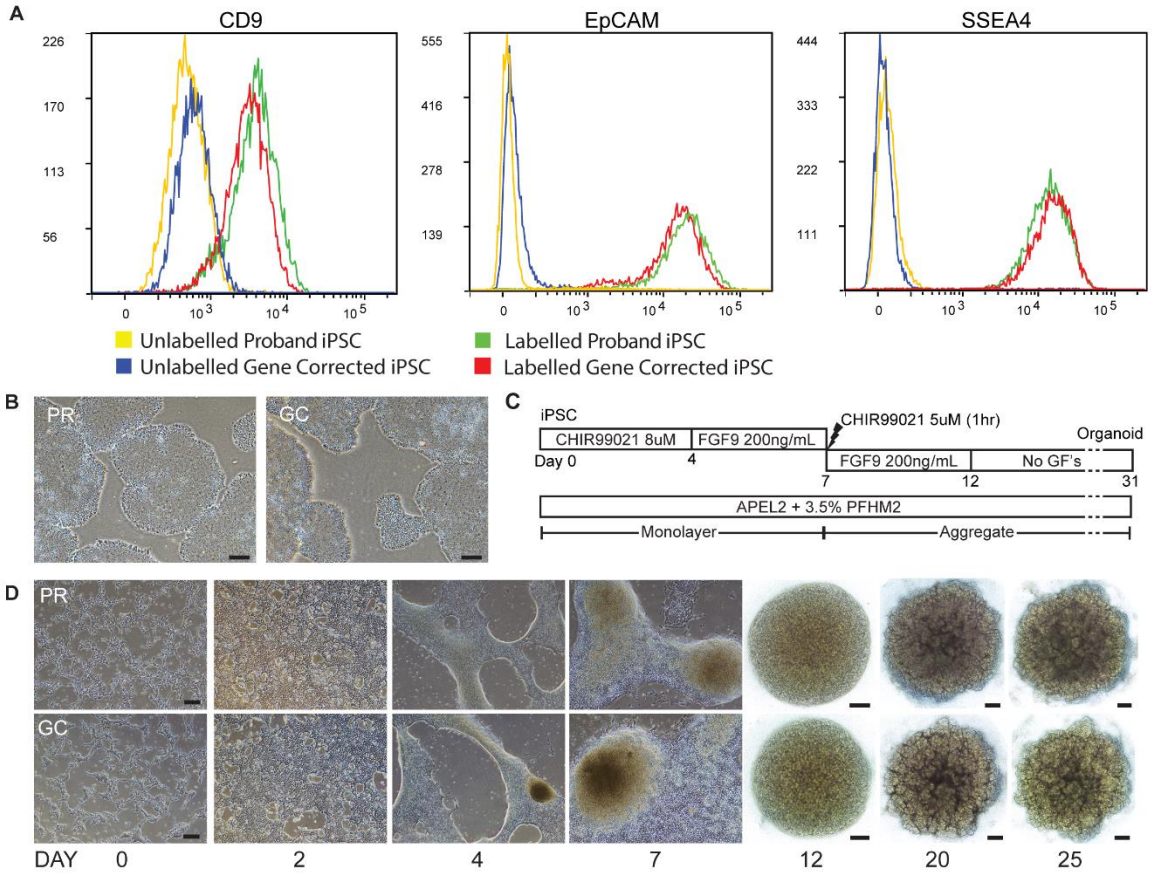

Figure S1. Pluripotency of iPSC Clones and Differentiation to Kidney Organoids.
(A) Pluripotency analysis of PR and GC iPSC clones. **(B)** Bright field images of PR and GC iPSC clones demonstrating iPSC morphology: tightly packed colonies with shiny edges. Scale bar 200um. **(C)** Differentiation protocol adapted from Takasato et al.[1] See methods section for details. **(D)** Bright field mages of differentiation demonstrate epithelial to mesenchymal transition between day zero and day four. Cultures become raised and rugated by day seven and self-organised structures are evident by day twelve, which mature with further culture. Monolayer scale bar 200um. Aggregate scale bar 500um.

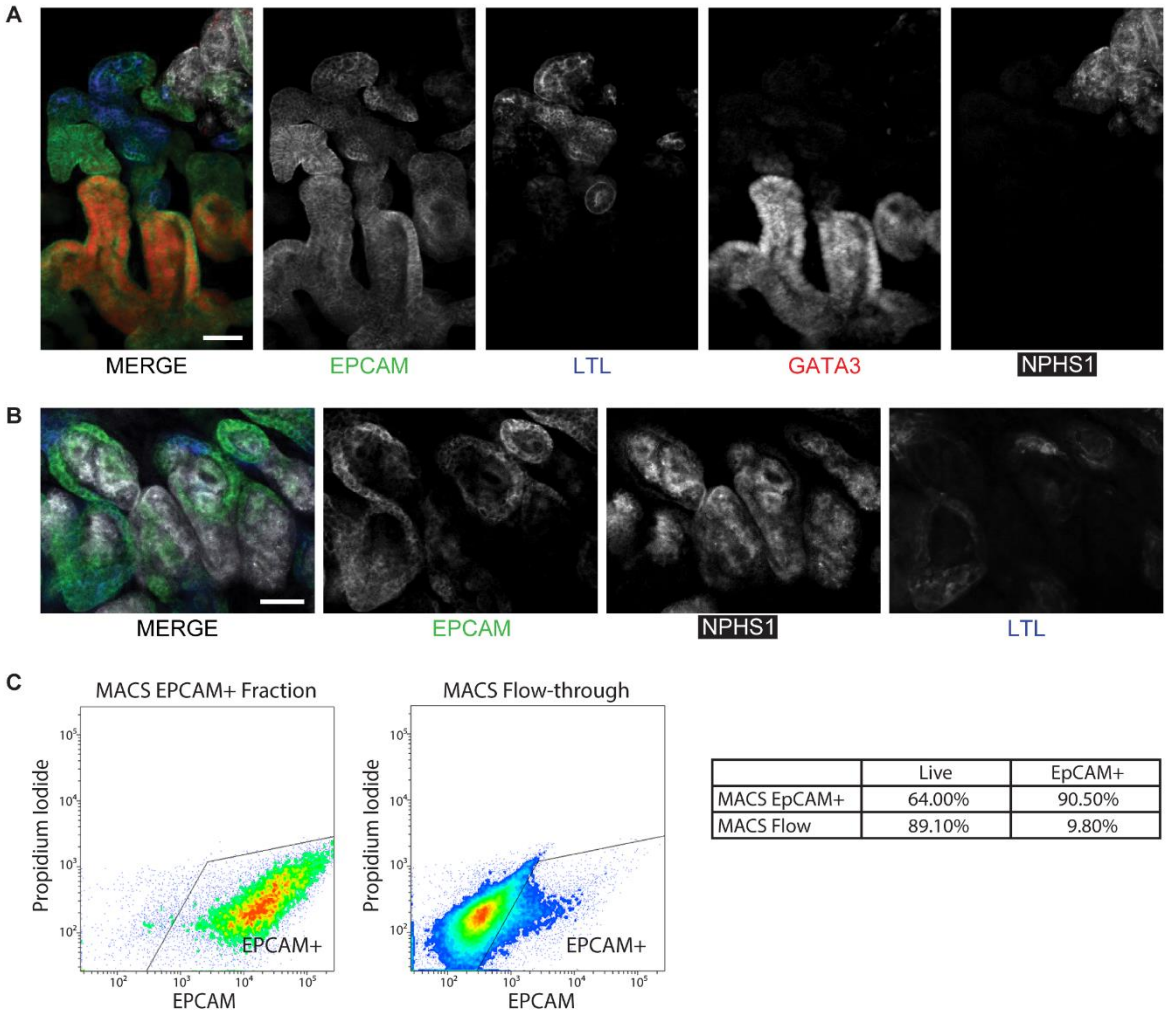

	Live	EpCAM+
MACS EpCAM+	64.00%	90.50%
MACS Flow	89.10%	9.80%

Figure S2. Characterisation and Validation of EPCAM MACS Sorting.
(A) Immunofluorescent validation of the cell populations that represent the EPCAM positive fraction of organoids. EPCAM conjugated with Alexafluor-488 (green) co-immunofluorescence with LTL+ proximal tubule (blue) and GATA3+ collecting duct (red) with a contiguous tubular structure between (distal tubule, reliably CDH1+ in other staining protocols). (Scale bar 50um) **(B)** NPHS1+ podocytes (white) are EPCAM negative but a rim of EPCAM+ cells surrounding glomerular structures resembles Bowman's capsule. (Scale bar 50um) **(C)** Flow cytometry of MACS sorted kidney organoids additionally incubated with EPCAM conjugated with Alexafluor-488 antibody demonstrates 64% viability in the eluted cell fraction which is 90.5% EPCAM+.

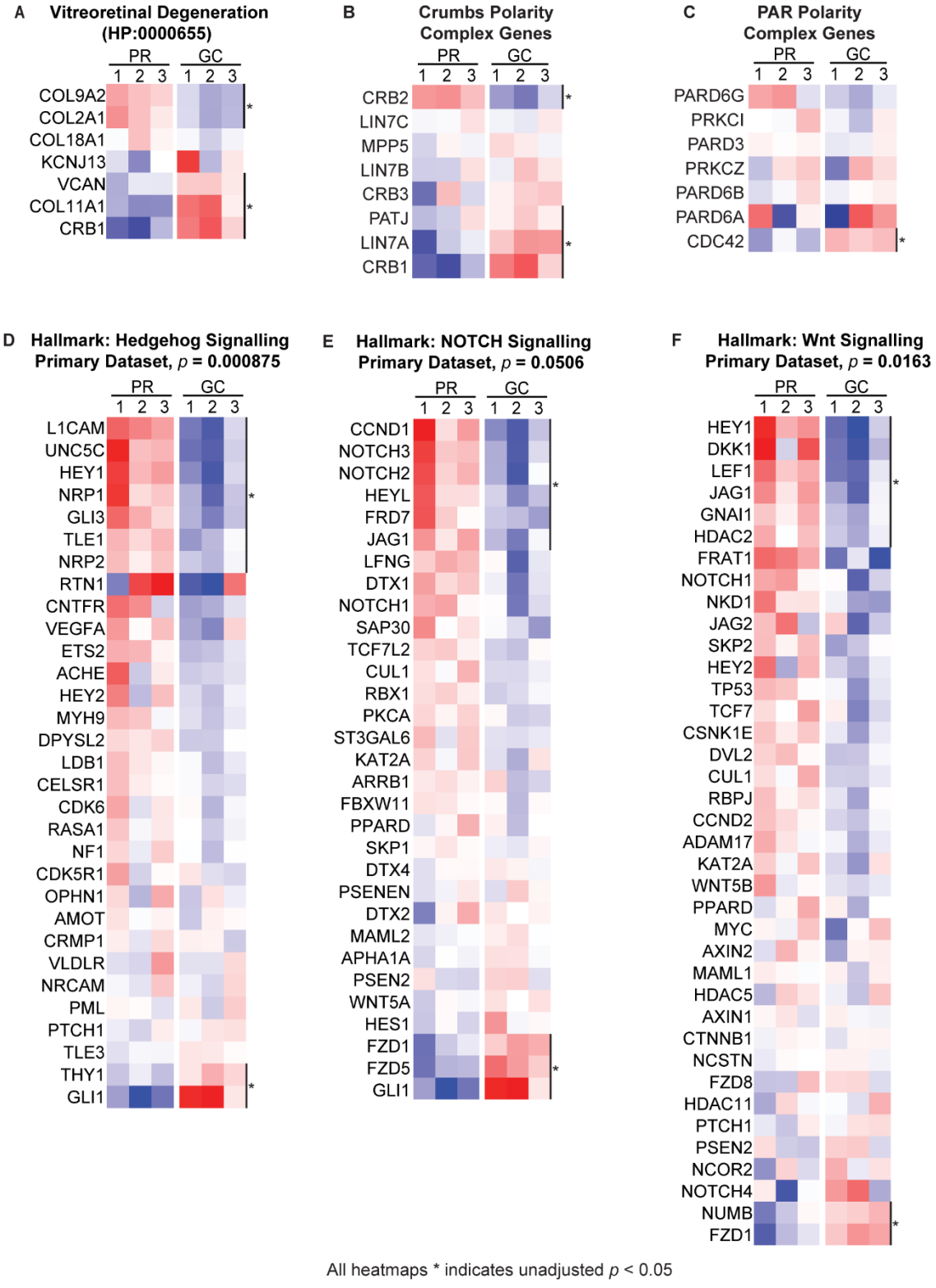

Figure S3. Differential Expression within Polarity and Cell Signalling Pathways. Heatmaps summarising DGE within primary RNASeq dataset **(A)** Human Phenotype term Vitreoretinal degeneration, **(B)** Crumbs polarity complex genes, **(C)** Par Polarity complex genes, **(D)** Hallmark Hedgehog signalling gene list, **(E)** Hallmark NOTCH signalling gene list, **(F)** Hallmark Wnt beta Catenin signalling gene set. Individual genes with significant DGE (i.e. $p < 0.05$) indicated by *.

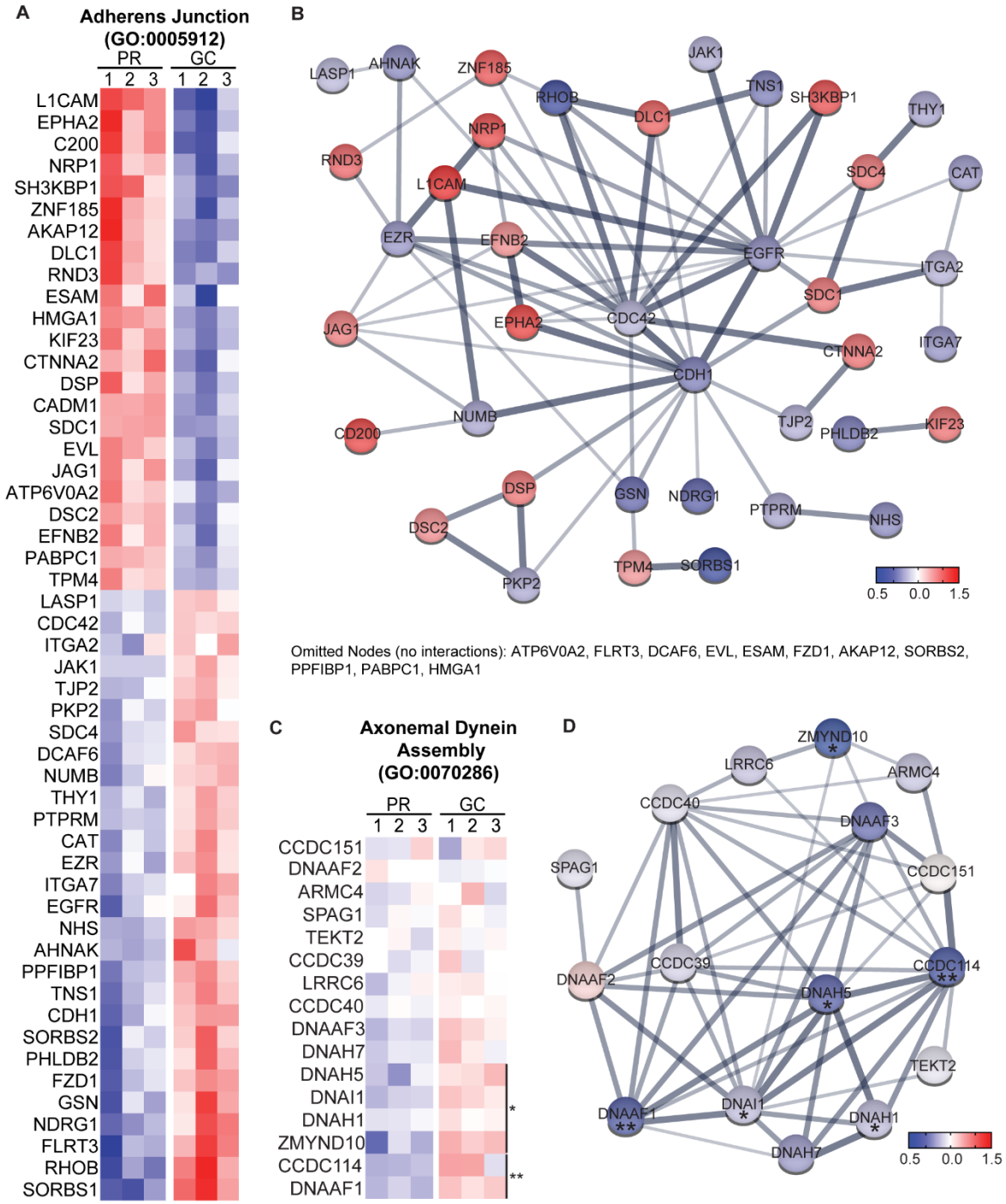

Figure S4. Differential Expression within Adherens Junction and Axonemal Dynein Assembly GO Terms with STRING Protein Interactomes.
(A) Heatmap demonstrating differential expression of genes from Adherens Junction GO Term (adjusted $p < 0.01$ for all genes). **(B)** STRING protein interactome of Adherens Junction DGE. Node colours represent average differential expression in of the PR triplicate relative to average of GC triplicate. Thickness of lines indicates strength of data supporting the shared function between the proteins. Protein nodes without interactions have been hidden. **(C)** Heatmap demonstrating differential expression of genes from Dynein Complex Assembly GO Term (* indicates adjusted $p < 0.05$, ** indicates adjusted $p < 0.01$). **(D)** STRING protein interactome of Dynein Complex Assembly DGE. Node colours represent average differential expression in of the PR triplicate relative to average of GC triplicate. Thickness of lines indicates strength of data supporting the shared function between the proteins. No omitted nodes.

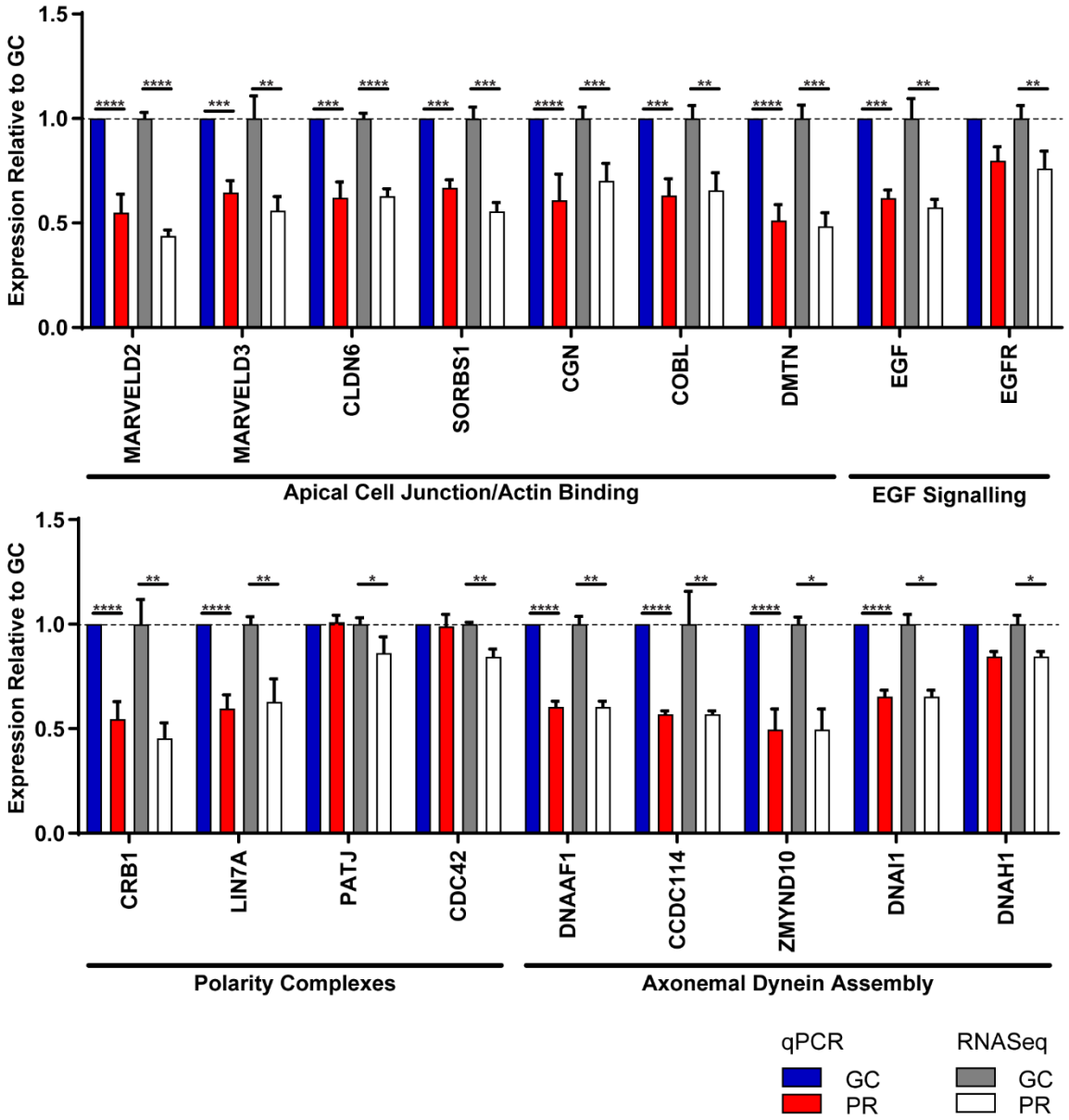

Figure S5. Validation of RNASeq by qPCR.
Quantitative real-time PCR (qPCR) of selected genes from RNA sequencing dataset. Genes were selected on the basis of adjusted *p* value and magnitude of read counts. For qPCR samples (GC blue; PR red) all PR values are graphed as 2^{-ddCT} and adjusted *p* values calculated by *t* test with Bonferroni-Dunn correction for multiple comparisons. For RNA sequencing samples (GC dark grey, PR light grey), all values were normalised to mean GC count and adjusted *p* values represent those from original bioinformatics analysis. (error bars represent standard error of the mean, * indicates adjusted $p < 0.05$, ** indicates adjusted $p < 0.01$, *** indicates adjusted $p < 0.001$, **** indicates adjusted $p < 0.0001$).

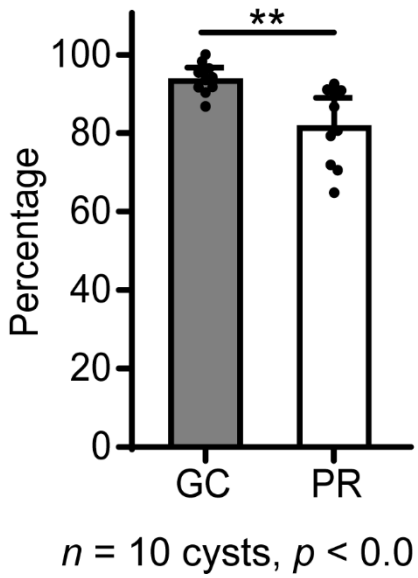

Figure S6. Cilia per Nucleus Measure from Epithelial Cyst Culture.
Mean cilia per nucleus counts from cyst culture demonstrate small but significant reduction in ciliation in PR cysts compared to GC cysts (PR 83.7% [74.7-89.3], GC 93.8% [91.1-96.7]; $p < 0.01$; error bars represent 95% confidence interval).

Table S1: Variant details, predicted impact and classification.

	Variant 1	Variant 2
Genomic position (hg19)	chr16:1612009 G > C	chr16:1642177 C > T
cDNA	NM_014714.3:c.2176C> G	NM_014714.3:c.634G> A
Predicted effect	p.(Pro726Ala)	p.(Gly212Arg) and/or splicing defect.
dbSNP ID	rs1057518064	rs201188361
Inheritance	Maternal	Paternal
Population frequency[a]	4.1x10-6 (AC=1)	5.4x10-5 (AC=15)
Damage prediction scores: - Polyphen - MutationTaster - CADD	 1.0 1.0 23.9	 0.91 1.0 27.4
Predicted splicing impact[b]	na	Broken WT Donor Site (score: -11.59)
ACMG Classification (evidence codes[c])	Likely Pathogenic (PM2, PM3, PP2, PP3, PP4 and PP5)	Pathogenic (PS1, PS3, PM2, PP2, and PP3)

a: gnomAD database, http://gnomad.broadinstitute.org [2]

b: Human Splicing Finder web service, http://www.umd.be/HSF3/index.html [3]

c: PS, pathogenic strong; PM, pathogenic moderate; PP, pathogenic supporting [4]

Table S7: Oligonucleotide Primers used for Real Time PCR

Gene	Forward Primer (5' to 3')	Reverse Primer (5' to 3')
MARVELD2	ACAACAGGAGTGTGAAATGGC	TCGGGCATCACGATAGGTTTAG
MARVELD3	ATTACCAGTCAGAGGCGGAAGG	CCAGGATCAGCAAGTTCAGGAG
CLDN6	AATTTCCCTTATCTCCTTCGC	GACTCCCAGGATCTGCATTC
SORBS1	CCCACCACCTTAAACCACTG	ATCCATGTCTTTGTCTTGCC
CGN	AGAAGCGTTTGCTGGACAGG	GCAGGGCTTGCTTAGAGTCC
COBL	CTGTGCAAGACAAGGCATCG	TTATCCTCAGTGCGGTTGGG
DMTN	GACCGGACACCCTTCCATAC	CCCTGATGGGCTGAACTCTG
EGF	TCCTGAAGGCTCAGTGCTTG	GGGCTAAGAGGAACGCAGAG
EGFR	GGTGCAGGAGAGGAGAACTG	ACTGGTTGTGGCAGCAGTC
CRB1	CTACAATGGAGGCAACTGCAC	GAGTAAGTCCTGGCACAGACC
LIN7A	GGCAACAGCAAAGGTATTCTCG	TGGGAGTGGCCTTCACTAGC
PATJ	TAGAGATGAGGCACACTACCG	CTCCGCTTCCATTTCGTTTC
CDC42	CTGAAGGCTGTCAAGTATGTGG	GGCTCTTCTTCGGTTCTGGAG
DNAAF1	ACAGGCAAATCTCTGGAAGACC	GCACAGGGAGTGACGTGTAG
CCDC114	ACAGCTGGAGAAGCTCAAGG	CTGGTCTTGACCCCAAGGAG
ZMYND10	GCCTCGATATGGGAGACCTG	GGATGGCTTGCATGTTCAGC
DNAI1	AGTCTGGCAAGCACTCAGAC	ATCCTGCCGTCAGATGACAC
DNAH1	GGAACCCTGTGAAGATCCG	TCGTGTTTCGGCTATGGAC
IFT140	CCGACTTCTTCATCGAGCACAG	ACGGTCATCTTTTCCGCCATC

Supplemental References

1. Takasato, M., Er, P.X., Chiu, H.S., and Little, M.H. (2016). Generation of kidney organoids from human pluripotent stem cells. Nat Protoc 11, 1681-1692.
2. Lek, M., Karczewski, K.J., Minikel, E.V., Samocha, K.E., Banks, E., Fennell, T., O'Donnell-Luria, A.H., Ware, J.S., Hill, A.J., Cummings, B.B., et al. (2016). Analysis of protein-coding genetic variation in 60,706 humans. Nature 536, 285-291.
3. Desmet, F.O., Hamroun, D., Lalande, M., Collod-Beroud, G., Claustres, M., and Beroud, C. (2009). Human Splicing Finder: an online bioinformatics tool to predict splicing signals. Nucleic Acids Res 37, e67.
4. Richards, S., Aziz, N., Bale, S., Bick, D., Das, S., Gastier-Foster, J., Grody, W.W., Hegde, M., Lyon, E., Spector, E., et al. (2015). Standards and guidelines for the interpretation of sequence variants: a joint consensus recommendation of the American College of Medical Genetics and Genomics and the Association for Molecular Pathology. Genet Med 17, 405-424.